

Low-loss millimeter-wave resonators with an improved coupling structure

A Anferov¹², S P Harvey³⁴, F Wan³⁴, K H Lee¹², J Simon³
and D I Schuster³⁴

¹ James Franck Institute, University of Chicago, Chicago, IL 60637, USA

² Department of Physics, University of Chicago, Chicago, IL 60637, USA

³ Department of Applied Physics, Stanford University, Stanford, CA 94305, USA

⁴ SLAC National Accelerator Laboratory, Menlo Park, CA, 94025 USA

E-mail: dschus@stanford.edu, aanferov@uchicago.edu

6 November 2023

Abstract. Millimeter-wave superconducting resonators are a useful tool for studying quantum device coherence in a new frequency domain. However, improving resonators is difficult without a robust and reliable method for coupling millimeter-wave signals to 2D structures. We develop and characterize a tapered transition structure coupling a rectangular waveguide to a planar slotline waveguide with better than 0.5 dB efficiency over 14 GHz, and use it to measure ground-shielded resonators in the W band (75 - 110 GHz). Having decoupled the resonators from radiative losses, we consistently achieve single-photon quality factors above 10^5 , with a two-level-system loss limit above 10^6 , and verify the effectiveness of oxide removal treatments to reduce loss. These values are 4-5 times higher than those previously reported in the W band, and much closer to typical planar microwave devices, demonstrating the potential for low-loss on-chip millimeter wave quantum technology.

Keywords: Millimeter-wave, W-band, Niobium, Superconducting resonator, Quantum measurements, Two level system loss, Waveguide finline transition

1. Introduction

Extending superconducting quantum device functionality to millimeter-wave frequencies (near 100 GHz) offers new opportunities for detection and transduction [1] and access to large coupling strengths for hybrid experiments [2, 3]. Most importantly, the reduced sensitivity to thermal noise of higher-energy mm-wave photons could enable quantum experiments at liquid-helium-4 temperatures, which significantly reduces cooling complexity and power dissipation constraints, enabling new pathways for scaling up quantum computing platforms, and could facilitate direct integration with high-speed superconducting digital logic. In order to establish more robust quantum information systems, it is vital to understand and minimize decoherence in superconducting devices. Significant effort has gone towards investigating and reducing sources of loss at microwave frequencies [4], establishing that a significant remaining contribution to decoherence at the single photon level comes from two-level-systems (TLS) found in amorphous dielectric materials. However, since probing individual decoherence mechanisms requires reducing other sources of loss, the nature and limits of TLS loss contributions and their frequency dependence when scaled to millimeter-wave frequencies remain relatively unexplored.

When measured at single-photon energies, the internal quality factor (Q_i) of an on-chip resonant circuit provides insight into the maximum coherence of a quantum system formed by adding a source of nonlinearity (such as kinetic inductance [5, 6] or a high-frequency Josephson junction [7, 8]). Significant progress has been made in improving millimeter-wave resonators [5, 6, 9–12], but their single-photon quality factors remain below $2\text{--}4 \times 10^4$: significantly lower than those measured in microwave circuits [13]. This can largely be attributed to two primary factors: first, millimeter-wave resonators frequently use substrates with low dielectric constants (such as SiO_2) to simplify high-frequency circuit design, despite their poor dielectric loss characteristics compared to crystalline silicon or sapphire. Second, many existing millimeter-wave resonators rely on coplanar stripline or microstrip transmission line components, both of which have relatively high radiation profiles resulting in increased radiative losses, particularly at high frequencies [14].

Taking inspiration from low-loss microwave de-

vices, a ground-shielded circuit design minimizing radiative loss offers an attractive method for increasing millimeter-wave quality factors, and better control over on-chip signal propagation and coupling. Whereas low-frequency signals can be routed to an on-chip waveguide directly through wire bonds, grounded circuits present additional design challenges in millimeter-wave bands, where signals are primarily transmitted by hollow waveguides, so require a method to efficiently direct the waveguide electromagnetic fields onto the chip. This proves to be a challenging problem, and as a result, a variety of transition structures coupling waveguides with on-chip transmission lines have been developed [15]; however, with no universal solution, transitions for specific applications are still actively studied and improved.

In this work, we use a transition specifically designed to measure ground-shielded superconducting millimeter-wave resonant circuits with improved control. We characterize a tapered coupling structure that efficiently confines the signal fields to an on-chip slotline waveguide, finding an insertion loss better than 0.5 dB over 14 GHz of bandwidth. We study niobium resonators patterned near the slotline and show that resonator coupling can be controlled independently without increasing radiation loss. With this novel superconducting resonator design combined with fabrication procedure, we improve on existing planar millimeter-wave devices and achieve high internal quality factors (Q_i) consistently exceeding 10^5 at single photon powers. This allows us to study the effects of oxide growth and removal on remaining loss contributions to Q_i from millimeter-wave two-level systems (TLS), and show that limits from TLS can be increased as high as 10^6 .

2. Tapered Waveguide Transition Design

When designing a millimeter-wave circuit to minimize loss, additional constraints apply to its coupling structure. Crystalline sapphire is an ideal substrate choice as it yields much lower dissipation than most dielectrics, but is more difficult to machine which imposes design limitations. As a result, transition designs requiring abnormally cut non-rectangular substrates [16–18], micromachining [19] or drilled holes [20] are impractical. Sapphire also presents additional challenges for high frequency circuit design due to its relatively high dielectric constant, which leads

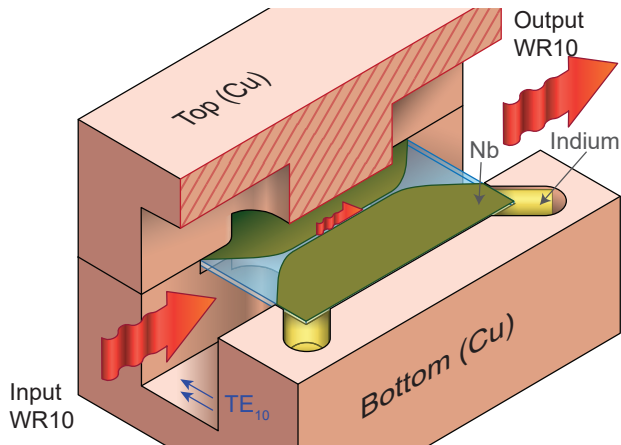


Figure 1. Cutaway diagram showing assembled back-to-back waveguide to on-chip slotline transition structures, with signal propagation marked in red. In the slotline region the waveguide geometry is constricted to prevent spurious propagating modes. On the chip corners, rounded channels allow indium wire (yellow) to deform, which secures the chip in place.

to more pronounced impedance mismatches caused by the presence of substrate in the waveguide [21]. Ensuring currents are carried by superconducting materials minimizes conduction loss. To achieve this, on-chip superconducting layers should be well separated from both waveguide and housing metal [22]: this consideration makes transitions with stripline geometries, which needs an external ground plane [23], less ideal. While potentially offering low radiation loss, coplanar waveguide transitions [19, 24] are typically more complex, requiring multiple stages and more physical space. Finline transitions, on the other hand, consist of a single taper [17, 18, 25], making them more compact, and transform the signal into a differential mode localized on the chip surface.

Table 1. Optimized taper dimensions used (in mm).

H_0	L_1	L_2	L_3	T_0	H_1	D_1	D_2
2.54	3.45	2.27	1.66	0.1	0.4	0.2	0.412
W_0	W_1	W_2	S_1	A_1	D_0	D_3	
1.27	2.29	2.11	0.04	0.895	0.55	0.8	

Our transition is defined by a superconducting niobium film patterned on the top surface of a rectangular crystalline sapphire substrate centered in a rectangular waveguide. Inspired by Refs. [17, 20, 25], the geometry consists of a differential unilateral finline that tapers from the waveguide width down to a narrow slotline. A cutaway diagram of the complete structure is shown in Figure 1, with two transitions coupled back-to-back by a length of on-chip slotline useful for coupling to resonators. Where the

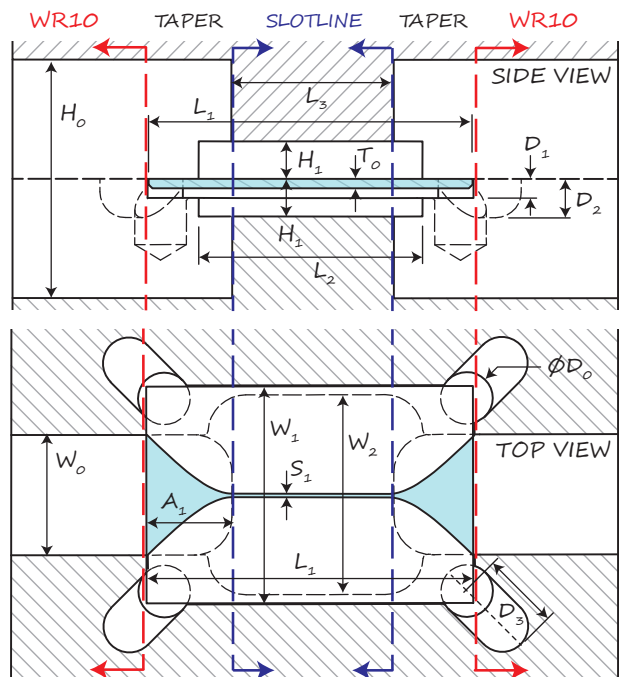


Figure 2. Side and top section views of the transition structure geometry, with reference planes and relevant dimensions marked. Un-metallized sections of the chip are shown in blue. The rounded corner channels are completely filled by indium.

transition terminates, the waveguide height is reduced to increase the cutoff frequency of unwanted higher-order propagating modes, while the waveguide width is broadened to increase the usable area of the chip: this allows the device area to remain suspended away from metal surfaces, which minimizes conduction loss [22]. The only direct contact with the copper enclosure occurs where the chip is clamped at its corners.

Due to the pronounced impedance discontinuity between the sapphire chip and the waveguide [21], a broadband matching structure is difficult to achieve with an exponential or cosine Vivaldi taper contour as is typically used in finline transitions [20, 25]. Instead, we find that a curved taper shape with a nearly linear waveguide entrance can compensate for the mismatch and can be optimized to give good performance over a section of waveguide bandwidth. The optimized contour is described by the function:

$$y(x) = \left(\frac{W_0 - S_1}{2} \right) \frac{x}{A_1} \sqrt{2 - \left(\frac{x}{A_1} \right)^2} \quad (1)$$

where W_0 is the smaller waveguide dimension, S_1 is the slotline width, and A_1 is the transition length. The geometry of the transition is detailed in Figure 2. Using finite element method simulation software[‡], the above contour function and parameterized geometry dimensions are optimized for maximal transmission

[‡] Ansys HFSS

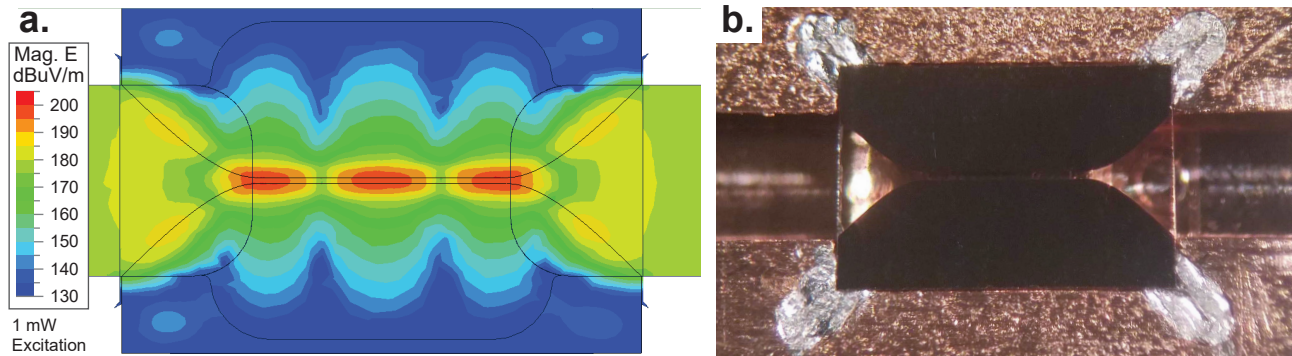


Figure 3. **a)** Simulated electric field distribution (log scale) viewed from the top for a wave traveling through the structure. Notably, a much greater dynamic range of electric field strengths is achieved as the signal is compressed into the slotline, as compared to just the waveguide field. **b)** Photograph of a mounted chip with back to back transition structures, with top copper block removed. The indium, visible on the corners of the chip, deforms and fully fills the designated channels, thermalizing and securing the chip.

in the 90-100 GHz band. The resulting optimal dimensions are listed in Table 1. Notably, by relaxing the bandwidth optimization constraint, we achieve a taper structure less than 0.9 mm long: much smaller than the $\lambda/2$ value predicted with analytical functions [21] and more compact than many other transition structures in literature [17, 18, 20, 25, 26].

The benefit of coupling to resonant devices through an intermediate on-chip slotline transmission line is apparent when examining the magnitude of the electric field of a wave propagating through the structure, shown in Figure 3a. Whereas some previous implementations of millimeter-wave resonators [5, 6] interact with a uniform waveguide electric field (visible on the left and right ends of Figure 3a) and rely on varying resonator dipole moments to adjust coupling, our method compresses the signal to a 40 μm slotline resulting in over 50 dB of dynamic range in electric field strength across the usable area of the chip. Consequently, the dipole coupling strength for each resonator can be set by its location on the chip, without needing to adjust the resonator's dipole moment, leaving more freedom to optimize the resonator performance.

3. Waveguide Transition Characterization

The taper geometry described above is defined by chlorine reactive ion etching a 100 nm thick film of high-purity electron-beam-deposited niobium grown on a 100 μm thick crystalline C-plane sapphire substrate (see Appendix A for detailed procedure). Short sections of indium wire are used to secure and thermalize the chip to the copper waveguide enclosure, visible in a photograph of the mounted chip shown in Figure 3b. The edges of the on-chip taper structure match the waveguide dimensions, which enables visual alignment during mounting (necessary to maximize

coupling).

The assembled structure is then measured at 0.86 K in a helium-4 cryostat: using a vector network analyzer with millimeter-wave extension modules and a cryogenic low noise amplifier, we measure the complex response in transmission and reflection. Input attenuation and cryogenic isolators reduce thermal noise reaching the sample, enabling measurements in the single photon limit. With a calibration procedure, the effects of additional hardware on the input and output lines are removed, and de-embedded scattering parameters of the sample are recovered from cryogenic measurements. These methods are detailed in Appendix B.

The effectiveness of the taper transitions is tested by using transitions to convert a waveguide signal to a slotline and back. The measurement results are summarized in Figure 4 and Figure 5. We find the transition performs best between 87.6 – 102.4 GHz, exceeding the designed range, and define this 14.8 GHz wide frequency range as the useful operating band.

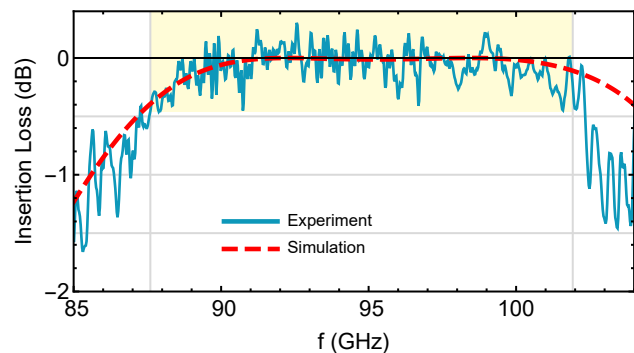


Figure 4. De-embedded insertion loss for two back-to-back transitions along with simulated values. In the band of interest (highlighted), we find an insertion loss better than 0.46 dB, limited by de-embedding calibration uncertainty (~ 0.3 dB).

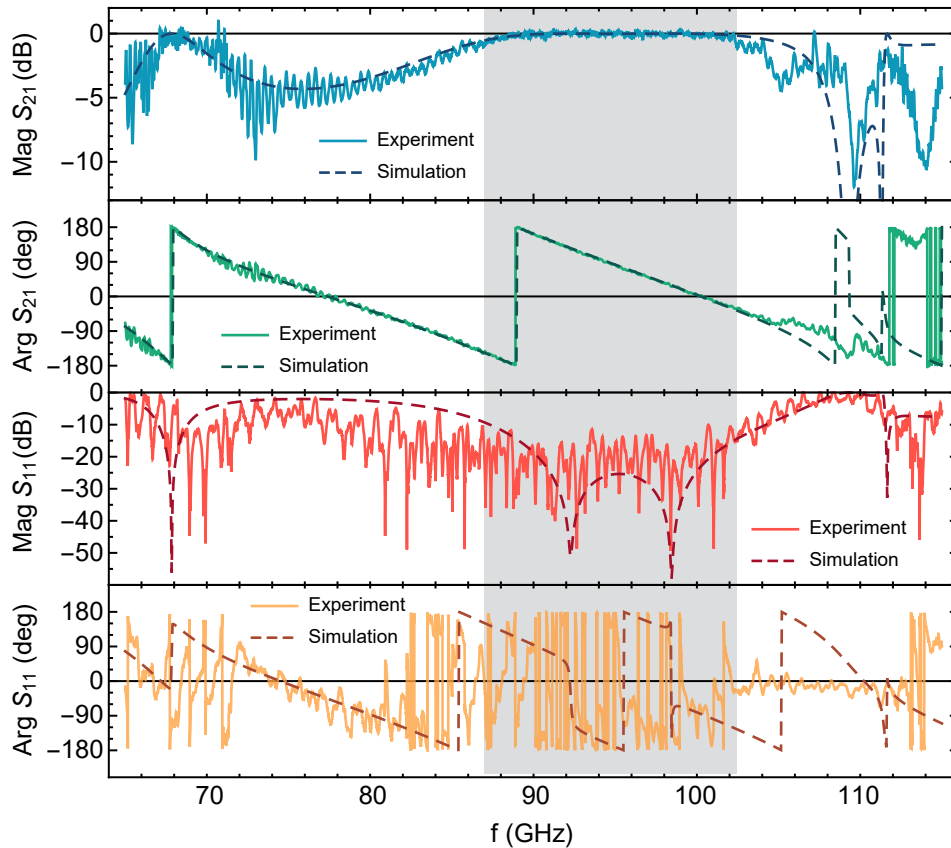


Figure 5. Wideband de-embedded scattering matrix parameter measurements (solid lines) for two transitions back-to-back along with respective simulations (dashed lines) showing good agreement. In the operating band marked in gray, we find a total insertion loss better than 0.5 dB, and return loss less than -13 dB.

Within the operating band, we find a maximum insertion loss of approximately 0.46 ± 0.35 dB (or 94.8% transmission), corresponding to a coupling efficiency of ~ 0.23 dB for a single taper structure. However these values are likely dominated by errors introduced by calibration methods (which do not enforce passivity).

Across the W band, we find that the de-embedded transmission and reflection of the structure are in fairly good agreement with simulations, with the exception of the region near 110 GHz: in this region unwanted resonances occur in the substrate and indium mounting regions, which are difficult to predict. In the operating band, we find the return loss exceeds 13.1 ± 8.6 dB, which slightly deviates from simulation, but could be attributed to the significantly increased calibration uncertainty due to the high transparency of the structure and increased sensitivity to error terms. Combined, these measurements demonstrate a transition structure in good agreement with simulation, which in the operating band couples a signal on and off a chip with high efficiency.

4. Ground-Shielded Resonator Design

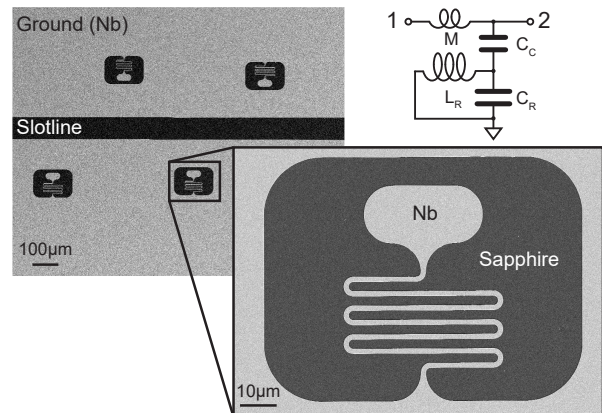


Figure 6. Electron micrograph of resonator geometry and coupling arrangement relative to feedline. This structure can be approximated by a simplified circuit diagram (top-right).

Having demonstrated a coupling structure capable of efficiently transforming a rectangular waveguide signal to and from a localized on-chip slotline, we can now design resonators decoupled from their

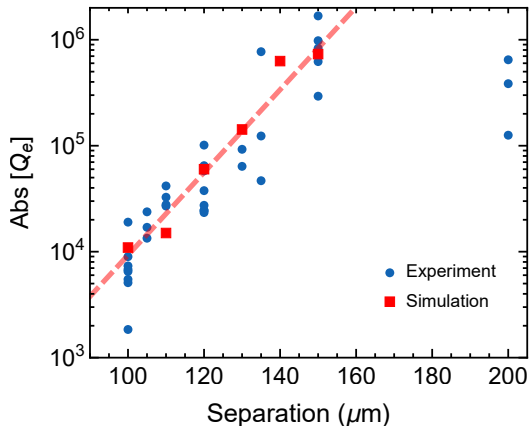


Figure 7. Simulated (red) resonator coupling Q_e as a function of separation from the slotline with an empirical fit (red line) used for predictions. Experimental measurements of Q_e (blue) are in reasonable agreement.

environment while only considering local interactions. Away from the centered slotline, the chip surface is entirely covered by superconducting material acting as a ground plane, so a resonant structure patterned in this region will have its long-range electric dipole interactions reduced. Our millimeter-wave resonator design is composed of a discrete capacitor island connected to the ground plane by a $2 \mu\text{m}$ -wide meandered inductor, shown in Figure 6. Every resonator is designed with an identical capacitor island, and its resonant frequency ω_0 is adjusted by changing the inductor length while keeping its width constant. The entire resonator has a rectangular footprint around $100 - 200 \mu\text{m}$ per side, which is not insignificant compared to signal wavelength in the slotline ($\sim 1 \text{ mm}$): in this limit, the ground plane edges contribute significant reactive corrections. On each chip, five to six resonators are placed near the central slotline to allow interaction with the propagating signal. This differential geometry can be modelled by the single-ended LC circuit shown in Figure 6 including asymmetric coupling (C_C and M) [27]. This accounts for reactive contributions and impedance mismatches induced by the resonator presence.

For this resonator geometry, coupling strength can be controlled by adjusting its separation from the slotline. The interaction decreases exponentially with distance, which we demonstrate by simulating the coupling quality factor Q_e as a function of resonator separation, plotted in red in Figure 7. The coupling quality factor can also be approximated empirically as a function of only the separation d by $\log_{10} Q_e = 0.06491 + 0.0390d/\mu\text{m}$, shown as a dashed line in Figure 7. We find that experimental measurements of Q_e (described in the next section) follow this approximation reasonably well.

5. Millimeter-wave Resonator Measurements

Characterizing the complex transmission spectra of these resonators at low temperatures ($T = 0.86 \text{ K}$) allows us to explore losses at millimeter-wave frequencies. Typical normalized measurements at low average photon number ($\bar{n} \approx 10$) are shown in Figure 8a. On resonance, we observe a dip in transmission as the resonance sweeps through a circle in the complex plane. This behavior is captured well by [27]:

$$S_{21} = 1 - \frac{Q}{Q_e^*} \frac{e^{i\phi}}{1 + 2iQ \frac{\omega - \omega_0}{\omega_0}} \quad (2)$$

where $Q^{-1} = Q_i^{-1} + \text{Re}[Q_e^{-1}]$ [27] and the coupling quality factor Q_e is rotated in the complex plane by $Q_e = Q_e^* e^{-i\phi}$ due to asymmetric coupling to the slotline as described in the previous section. Measuring both quadratures of the transmission spectrum to capture this asymmetry is particularly important for extracting an accurate estimate of Q_i , which is sensitive to ϕ [28]. This is noticeable in Figure 8d, which shows the same measurements performed on a different resonator with a higher degree of asymmetry that is successfully captured by Equation 2.

Repeating these measurements at varying powers shows that Q_i increases with power, as shown in Figure 8b. This increase can be explained by a power-dependent loss mechanism from saturating TLSs [29–32] described by:

$$Q_{\text{TLS}}(\bar{n}, T) = \frac{Q_{\text{TLS},0}}{\tanh \frac{\hbar\omega}{kT}} \sqrt{1 + \left(\frac{\bar{n}}{n_c}\right)^\beta \tanh \frac{\hbar\omega}{kT}} \quad (3)$$

Here $Q_{\text{TLS},0}$ is the inverse linear absorption from TLSs, ω is the resonant frequency, and β and n_c are parameters characterizing TLS saturation [29, 32]. Nonlinear effects (from kinetic inductance) [6] limit the power range where linear measurements can be performed, however at high powers we observe that Q_i begins to saturate, indicating the presence of other loss mechanisms.

By examining the power and temperature dependence of Q_i , we can further distinguish between sources of loss. The full behavior is captured with a model that includes TLS loss (Q_{TLS}) [29–32], equilibrium quasiparticle loss (Q_σ) [33–35] and other loss mechanisms that are power and temperature-independent (Q_{other}):

$$\frac{1}{Q_i(T, \bar{n})} = \frac{1}{Q_{\text{TLS}}(\bar{n}, T)} + \frac{1}{Q_\sigma(T)} + \frac{1}{Q_{\text{other}}} \quad (4)$$

The quasiparticle loss term is parameterized by:

$$Q_\sigma(T) = Q_{\sigma_0} \frac{\sigma_2(T, T_c)}{\sigma_1(T, T_c)} \quad (5)$$

where σ_1 and σ_2 respectively are the real and imaginary parts of the complex surface conductance,

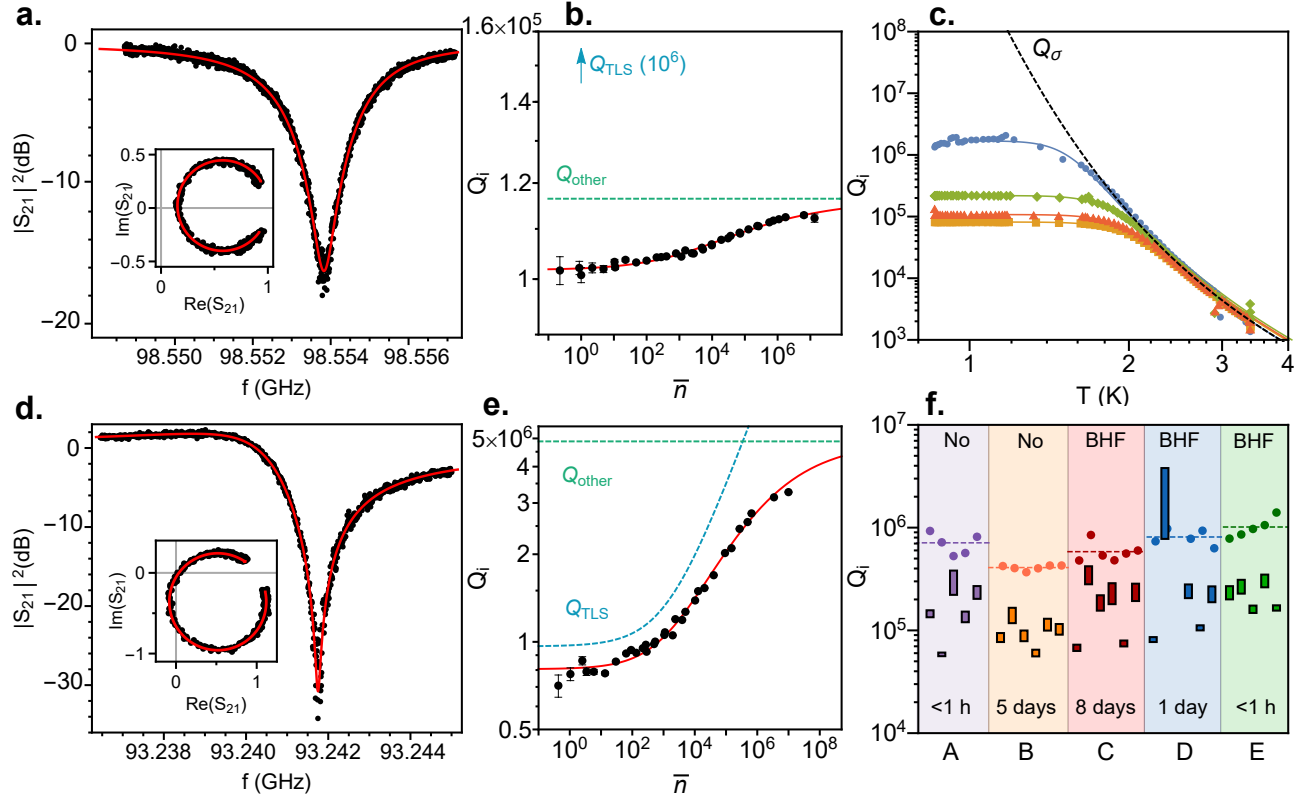


Figure 8. **a-b)** Complex transmission spectrum of a typical resonator, and power dependence of its internal quality factor along with fits to a model including TLS and independent loss (red). Here, Q_i is primarily limited by non-TLS loss (Q_{other}). **c)** Temperature dependence of Q_i for resonators from chip D. The black dashed line corresponds to a Bardeen-Cooper-Schrieffer (BCS) model of conductivity loss, and solid lines are respective fits to a model including conductivity and TLS loss. **d-e)** Complex transmission spectrum and Q_i power dependence of the best resonator measured in this study. For this device, Q_{TLS} is the dominant loss source. **f)** Internal quality factors for resonators in this study, grouped by etching conditions and elapsed time after fabrication. The top and bottom of the colored bars correspond to measured low-power and high-power limits of Q_i , and the points correspond to TLS induced loss $Q_{\text{TLS},0}$ with averages for each chip denoted by a dashed line.

calculated by numerically integrating the Mattis-Bardeen equations for σ_1/σ_n and σ_2/σ_n , and σ_n is the normal conductance. [33–35].

To investigate the effects of quasiparticle loss, we measure Q_i of several representative resonators as a function of temperature and show the results in Figure 8c along with $Q_\sigma(T)$ and fits to the full model described above. Below approximately 1.5 K we find that Q_i is almost unaffected by Q_σ and is nearly temperature independent for most devices. As the temperature approaches a significant fraction of niobium’s critical temperature (9.2 K), Q_σ rapidly becomes dominant. However, at the low temperatures relevant for quantum experiments, Q_σ exceeds measured values of Q_i by several orders of magnitude, suggesting that quasiparticle loss contributions are negligible in this regime.

Having determined that the dominant loss contributions come from power-independent loss Q_{other} and Q_{TLS} , we can neglect thermal contributions to Q_i at low temperatures. Upon inspection of the power

dependence of a typical resonator in Figure 8b, we find the increase of Q_i from TLS saturation is relatively small, unlike what is seen in many microwave loss studies [36, 37]. Using the model above, we find $Q_{\text{TLS},0} = 0.953 \times 10^6$ while $Q_{\text{other}} = 1.17 \times 10^5$, indicating that TLSs are not the dominant loss source. Repeating these measurements for the highest-Q resonator in this study, we find in Figure 8d that Equation 2 is able to accurately capture Q_i from the response, but unlike the other resonators, the power dependence shown in Figure 8e is much more pronounced. For this device, we find single-photon $Q_i = 0.827 \times 10^6$, which is comparable to state-of-the-art microwave resonators [36, 37], and the loss sources can be disentangled into $Q_{\text{TLS},0} = 1.03 \times 10^6$ and $Q_{\text{other}} = 4.18 \times 10^6$. Unlike the device above, this independent loss limit is significantly higher and the resonator loss primarily arises from Q_{TLS} , giving us a better insight into millimeter-wave TLS loss.

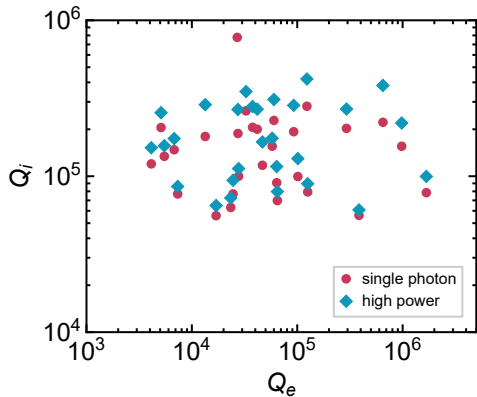


Figure 9. Resonator loss (internal Q) for single-photon (red) and high-powers (blue) as a function of coupling Q , showing no correlation and confirming coupling does not increase loss.

5.1. Reducing Losses With Surface Oxide Etch

When exposed to air, niobium is known to slowly evolve a lossy amorphous surface oxide layer containing dissipative sub-oxides [38] and TLSs [37]. Surface treatments are commonly used to remove this surface layer in microwave resonators to reduce loss [37]. Although TLS density has not yet been investigated in the W-band, losses from niobium sub-oxides are believed to be more pronounced at higher frequencies [38]. To study the effect of surface processing on Q_i , we repeat the measurements summarized in Fig. 8a-b for devices that underwent different aging times and etch conditions. In Fig. 8f, we plot the low and high power limits of measured Q_i as well as the fitted value of $Q_{\text{TLS},0}$ for devices from five separate chips.

Between samples A and B we observe that 5 days of aging reduces both $Q_{\text{TLS},0}$ and Q_{other} , leading to lower quality factors for resonators exposed to air for several days, which is consistent with niobium oxide regrowth that has been shown to increase loss in microwave devices [37]. This can be mitigated by selectively removing the surface layer of niobium oxide after fabrication using a buffered solution of hydrogen fluoride (BHF) [37], which we achieve by immersing samples C, D and E in a 5% BHF solution for 40 min immediately prior to mounting and measurement.

We observe that this BHF treatment can reverse the effects of air exposure in Sample C, which despite experiencing a longer air exposure of 8 days, has higher average $Q_{\text{TLS},0}$ and Q_{other} than Sample B after the BHF treatment. Applying this surface treatment to samples D and E, which experienced reduced initial air exposure yield consistently lower losses than samples A-C, including the highest- Q resonator in this study described above. Combining minimal air exposure with surface oxide removal using BHF in sample E, we are able to consistently obtain resonators with single

photon internal quality factors above 1.4×10^5 , and an average $Q_{\text{TLS},0} = 1.04 \times 10^6$: significantly higher than previously measured for planar millimeter-wave devices [5, 6, 9–12].

While these values of loss are much closer to those reported for microwave devices [37], in the power-dependent measurements above we observe that our millimeter-wave resonators are on average limited by power and temperature-independent loss Q_{other} to a much greater extent than TLS loss, which limits microwave devices [36, 37]. This loss could come from a variety of sources, including remnants of conduction loss from the copper enclosure [22], seam loss from an imperfect seal between the halves of the enclosure [39], radiation loss [40] or additional power-independent microscopic relaxation channels such as conductive loss in the niobium sub-oxides [37]. To estimate the impact of radiation losses, we can verify that our ground-shielded resonator design protects the resonance from radiative loss induced by coupling. In Figure 9 we plot Q_i for single-photon and high-power limits (Q_{other}) as a function of Q_e , and observe no correlation with either. Thus we can design a resonant circuit with a wide range of coupling strengths without affecting coupling to lossy or radiative channels. As a final note, an examination of all the devices in Figure 8f, shows that on average $Q_{\text{TLS},0}$ and Q_{other} scale similarly relative to each other when affected by aging and surface treatment. This is highly suggestive that the remaining millimeter-wave source of loss is still tied to materials-induced decoherence in the superconductor surface, and warrants further studies.

6. Conclusion

We have demonstrated an on-chip millimeter-wave resonator design with a ten-fold improvement in loss over previous work, and leveraged this platform to investigate sources of single-photon decoherence in the W band. Using a specifically-designed waveguide to slotline transition based on a finline taper, we present a new platform for probing on-chip devices at high frequencies. With this novel packaging design, we have improved on dipole coupling techniques previously used to address millimeter-wave resonators, and show that our coupling can be adjusted over a wide range without impacting circuit losses. Having shown that planar millimeter-wave resonators compatible with fabrication techniques can achieve performance comparable to microwave quantum circuits [36, 37], we pave the way for a millimeter-wave artificial atom that could be formed by introducing a high-frequency nonlinearity [6–8] into our design. This opens the door to a new generation of high-frequency quantum tools compatible with higher operating temperatures.

Acknowledgments

The authors thank P. Duda for assistance with fabrication process development, and M. W., A. Kumar and A. Suleymanzade for useful discussions. This work is supported by the U.S. Department of Energy Office of Science National Quantum Information Science Research Centers as part of the Q-NEXT center, and partially supported by the University of Chicago Materials Research Science and Engineering Center, which is funded by the National Science Foundation under Grant No. DMR-1420709. This work made use of the Pritzker Nanofabrication Facility of the Institute for Molecular Engineering at the University of Chicago, which receives support from Soft and Hybrid Nanotechnology Experimental (SHyNE) Resource (NSF ECCS-2025633).

References

- [1] Pechal M and Safavi-Naeini A H 2017 *Physical Review A* **96** 042305
- [2] Xiang Z L, Ashhab S, You J and Nori F 2013 *Reviews of Modern Physics* **85** 623–653
- [3] Clerk A A, Lehnert K W, Bertet P, Petta J R and Nakamura Y 2020 *Nature Physics* **16** 257–267
- [4] McDermott R 2009 *IEEE Transactions on Applied Superconductivity* **19** 2–13
- [5] Stokowski H, Pechal M, Snively E, Kevin Multani K S, Welander P B, Witmer J, Nanni E A and Safavi-Naeini A H 2019 Towards Millimeter-Wave Based Quantum Networks 2019 44th International Conference on Infrared, Millimeter, and Terahertz Waves (IRMMW-THz) pp 1–2
- [6] Anferov A, Suleymanzade A, Oriani A, Simon J and Schuster D I 2020 *Physical Review Applied* **13** 024056
- [7] Kim S, Terai H, Yamashita T, Qiu W, Fuse T, Yoshihara F, Ashhab S, Inomata K and Semba K 2021 *Communications Materials* **2** 98
- [8] Anferov A, Lee K H, Zhao F, Simon J and Schuster D I 2023 (*Preprint* 2306.05883)
- [9] Gao J, Vayonakis A, Noroozian O, Zmuidzinas J, Day P K and Leduc H G 2009 *AIP Conference Proceedings* **1185** 164–167
- [10] Shirokoff E, Barry P S, Bradford C M, Chattopadhyay G, Day P, Doyle S, Hailey-Dunsheath S, Hollister M I, Kovács A, McKenney C, Leduc H G, Llombart N, Marrone D P, Mauskopf P, O’Brien R, Padin S, Reck T, Swenson L J and Zmuidzinas J 2012 MKID development for SuperSpec: An on-chip, mm-wave, filter-bank spectrometer *Millimeter, Submillimeter, and Far-Infrared Detectors and Instrumentation for Astronomy VI* vol 8452 (SPIE) pp 209–219
- [11] Endo A, Sfiligoj C, Yates S J C, Baselmans J J A, Thoen D J, Javadzadeh S M H, van der Werf P P, Baryshev A M and Klapwijk T M 2013 *Applied Physics Letters* **103** 032601
- [12] U-yen K, Brown A D, Moseley S H, Noroozian O and Wollack E J 2017 *IEEE Transactions on Applied Superconductivity* **27** 1–4
- [13] McRae C R H, Wang H, Gao J, Vissers M R, Brecht T, Dunsworth A, Pappas D P and Mutus J 2020 *Review of Scientific Instruments* **91** 091101
- [14] Van Berkel S 2015 *Characterization of Printed Transmission Lines at High Frequencies* Master’s thesis TU Delft
- [15] Jastrzebski A, Yip J and Li D 2002 Waveguide packaging at mm-wave frequencies 14th International Conference on Microwaves, Radar and Wireless Communications. MIKON - 2002. Conference Proceedings (IEEE Cat.No.02EX562) vol 1 pp 121–135 vol.1
- [16] Valletti L, Fantauzzi S and Di Paolo F 2022 *Journal of Infrared, Millimeter, and Terahertz Waves* **43** 628–653
- [17] Yassin G, Grimes P K, King O G and North C E 2008 *Electronics Letters* **44** 866–867
- [18] Jing S, Fa-guo L, Li-hua H, Xiao-ying S and ZhengYan-qiu 2013 Waveguide-to-Microstrip Antipodal Finline Transition at W Band 2013 Third International Conference on Instrumentation, Measurement, Computer, Communication and Control pp 510–513
- [19] Lee Y, Becker J, East J and Katehi L 2004 *IEEE Transactions on Microwave Theory and Techniques* **52** 1001–1007
- [20] Al Henawy M and Schneider M 2012 Rectangular waveguide to coplanar stripline transition based on a unilateral finline 2012 6th European Conference on Antennas and Propagation (EUCAP) pp 405–409
- [21] Yip J, Jastrzebski A, Collier R and Li D 2002 The design of waveguide-to-finline taper transitions at millimetre wave frequencies 14th International Conference on Microwaves, Radar and Wireless Communications. MIKON - 2002. Conference Proceedings (IEEE Cat.No.02EX562) vol 1 pp 282–285 vol.1
- [22] Huang S, Lienhard B, Calusine G, Vepsäläinen A, Braumüller J, Kim D K, Melville A J, Niedzielski B M, Yoder J L, Kannan B, Orlando T P, Gustavsson S and Oliver W D 2021 *PRX Quantum* **2** 020306

- [23] Wu C, Zhang Y, Li Y, Zhu H, Xiao F, Yan B and Xu R 2022 *IEEE Transactions on Microwave Theory and Techniques* **70** 1087–1096
- [24] Mottonen V and Raisanen A 2004 *IEEE Transactions on Microwave Theory and Techniques* **52** 1836–1842
- [25] Giese M, Meinhardt T and Jacob A F 2015 Compact wideband single-ended and differential microstrip-to-waveguide transitions at W-band 2015 *IEEE MTT-S International Microwave Symposium* pp 1–4
- [26] Hung C F, Liu A S, Chien C H, Wang C L and Wu R B 2005 *IEEE Microwave and Wireless Components Letters* **15** 128–130
- [27] Khalil M S, Stoutimore M J A, Wellstood F C and Osborn K D 2012 *Journal of Applied Physics* **111** 054510
- [28] Probst S, Song F B, Bushev P A, Ustinov A V and Weides M 2015 *Review of Scientific Instruments* **86** 024706
- [29] Gao J 2008 *The Physics of Superconducting Microwave Resonators* Ph.D. thesis California Institute of Technology
- [30] Pappas D P, Vissers M R, Wisbey D S, Kline J S and Gao J 2011 *IEEE Transactions on Applied Superconductivity* **21** 871–874
- [31] Wang H, Hofheinz M, Wenner J, Ansmann M, Bialczak R C, Lenander M, Lucero E, Neeley M, O’Connell A D, Sank D, Weides M, Cleland A N and Martinis J M 2009 *Applied Physics Letters* **95** 233508
- [32] Sage J M, Bolkhovsky V, Oliver W D, Turek B and Welander P B 2011 *Journal of Applied Physics* **109** 063915
- [33] Reagor M J 2016 *Superconducting Cavities for Circuit Quantum Electrodynamics* Ph.D. thesis Yale University
- [34] Tinkham M 1996 *Introduction to Superconductivity* (Courier Corporation)
- [35] Mattis D C and Bardeen J 1958 *Physical Review* **111** 412–417
- [36] Crowley K D, McLellan R A, Dutta A, Shumiya N, Place A P M, Le X H, Gang Y, Madhavan T, Bland M P, Chang R, Khedkar N, Feng Y C, Umbarkar E A, Gui X, Rodgers L V H, Jia Y, Feldman M M, Lyon S A, Liu M, Cava R J, Houck A A and de Leon N P 2023 *Phys. Rev. X* **13** 041005 ISSN 2160-3308
- [37] Verjauw J, Potočnik A, Mongillo M, Acharya R, Mohiyaddin F, Simion G, Pacco A, Ivanov Ts, Wan D, Vanleenhove A, Souriau L, Jussot J, Thiam A, Swerts J, Piao X, Couet S, Heyns M, Govoreanu B and Radu I 2021 *Physical Review Applied* **16** 014018
- [38] Chang C L, Ade P A R, Ahmed Z, Allen S W, Arnold K, Austermann J E, Bender A N, Bleem L E, Benson B A, Carlstrom J E, Cho H M, Ciocys S T, Cliche J F, Crawford T M, Cukierman A, Ding J, de Haan T, Dobbs M A, Dutcher D, Everett W, Gilbert A, Halverson N W, Hanson D, Harrington N L, Hattori K, Henning J W, Hilton G C, Holder G P, Holzapfel W L, Hubmayr J, Irwin K D, Keisler R, Knox L, Kubik D, Kuo C L, Lee A T, Leitch E M, Li D, McDonald M, Meyer S S, Montgomery J, Myers M, Natoli T, Nguyen H, Novosad V, Padin S, Pan Z, Pearson J, Posada Arbelaez C, Reichardt C L, Ruhl J E, Saliwanchik B R, Simard G, Smecher G, Sayre J T, Shirokoff E, Stark A A, Story K, Suzuki A, Thompson K L, Tucker C, Vanderlinde K, Vieira J D, Vikhlinin A, Wang G, Yefremenko V and Yoon K W 2015 *IEEE Transactions on Applied Superconductivity* **25** 1–5
- [39] Brecht T, Reagor M, Chu Y, Pfaff W, Wang C, Frunzio L, Devoret M H and Schoelkopf R J 2015 *Applied Physics Letters* **107** 192603
- [40] Catelani G, Schoelkopf R J, Devoret M H and Glazman L I 2011 *Physical Review B* **84** 064517
- [41] Yeh J H and Anlage S M 2013 *Rev. Sci. Instrum.* **84** ISSN 0034-6748
- [42] Wang H, Singh S, McRae C R H, Bardin J C, Lin S X, Messaoudi N, Castelli A R, Rosen Y J, Holland E T, Pappas D P and Mutus J Y 2021 *Quantum Sci. Technol.* **6** 035015 ISSN 2058-9565
- [43] Cataldo G, Wollack E J, Barrentine E M, Brown A D, Moseley S H and U-Yen K 2015 *Rev. Sci. Instrum.* **86** ISSN 0034-6748
- [44] Pozar D M 2011 *Microwave Engineering* (John Wiley & Sons)

Appendix A. Device Fabrication

100 μm -thick C-plane polished sapphire wafers are annealed at 1200° C for 1.5 hours, and allowed to slowly cool to room temperature. Next the wafers are ultrasonically cleaned in toluene, acetone, methanol, isopropanol and de-ionized (DI) water, and finally etched in a piranha solution kept at 40° C for 2 minutes and rinsed with de-ionized water. Immediately following, the wafers are loaded into a Plassys MEB550S electron-beam evaporation system, where they are baked at >200° C under vacuum for an hour to help remove water and volatiles. When a sufficiently low pressure is reached ($< 5 \times 10^{-8}$ mBar), titanium is electron-beam evaporated to bring the load

lock pressure down even further. 100 nm of Nb is now deposited by first evaporating at > 0.5 nm/s while rotating the substrate. The substrate is allowed to cool in vacuum for several minutes, before exposing it to air.

The wafers are mounted on a silicon handle wafer using AZ1518 photoresist cured at 115°C , then coated with $1\mu\text{m}$ of AZ MiR 703 photoresist and exposed with a 375 nm laser in a Heidelberg MLA150 direct-write system. The assembly is hardened for etch resistance by a 1 min bake at 115°C then developed with AZ MIF 300, followed by a rinse in DI water. The resonators and/or finline structure is now etched in a chlorine inductively coupled plasma reactive ion etcher with Cl_2 , BCl_3 and Ar. The plasma conditions are optimized to be in the ballistic ion regime, which gives high etch rates with minimal re-deposition. Immediately after exposure to air, the wafer is quenched in DI water: this helps prevent excess etching by quickly diluting any surface HCl (formed by adsorbed Cl reacting with water vapor in the air). The remaining photoresist is thoroughly dissolved in a mixture of 80°C n-methyl-2-pyrrolidone with a small addition of surfactants, which also removes the substrate from the handle wafer.

With the superconducting structure complete, the wafer is ultrasonically cleaned with acetone and isopropanol, coated with a thick protective covering of photoresist (MiR 703) cured at 115°C , and diced into chips (see Table 1 for dimensions). The protective covering is now dissolved in 80°C n-methyl-2-pyrrolidone with surfactants (we find this can also help remove stubborn organic residues from previous steps), and the chips are given a final ultrasonic clean with acetone and isopropanol. The finished chips are stored in air for variable time (see main text for discussion) then packaged and cooled down.

Appendix B. Cryogenic Measurements and Calibration

Appendix B.1. Experimental Measurement Setup

All millimeter-wave characterization was performed in a custom built ^4He adsorption refrigerator, with a base temperature of 0.86 K, and a cycle duration of 3 hours. We generate millimeter-wave signals (75-115 GHz) at room temperature by sending microwave signals (12-19 GHz) into a frequency multiplier. The upconverted signal is sampled to establish a phase reference measurement. We convert the generated waveguide TE_{10} mode to a 1 mm diameter stainless steel and beryllium copper coaxial cable, which carries the signal to the 1 K stage of the fridge, thermalizing mechanically at each intermediate stage, then convert back to a WR-10 waveguide which leads to the device under test. The cables and waveguide-cable converters

have a combined frequency-dependent loss ranging from 38.6 dB to 49.8 dB in the W-Band, dominated by the cable loss. In the case of a transmission measurement, the signal is further thermalized to 1 K by a cryogenic 20 dB attenuator, and in the case of a reflection measurement, this thermalization is accomplished with a 20 dB cryogenic directional coupler with a copper body. The sample is thermally isolated from the 1 K stage of the refrigerator to allow local heating for temperature sweeps.

Wideband cryogenic millimeter-wave circulators are currently not commercially available, so instead a cryogenic directional coupler allows enables reflection measurements by allowing nearly all of the reflected and transmitted signal to pass through to a low noise amplifier. Cryogenic faraday isolators minimize retro-reflections and prevent thermal radiation from leaking in on the output side, while still allowing good transmission. Having passed outside the cryostat through custom-built hermetic adapters, the signal is downconverted and amplified for measurement. The entire setup is summarized in Figure B1a-b.

Appendix B.2. Cryogenic Calibration

The cryogenic measurements described above introduce a complex network between the sample and the measurement equipment, a calibration must be performed to obtain accurate estimates of network parameters. The necessity of attenuating components as well as active components with gain in the measurement chain make cryogenic calibrations a complex problem [41–43]. Without access to a cryogenic millimeter-wave switch that can instantly select a calibration standard in-situ, we instead rely on a standard TRL-type calibration [44] with carefully controlled sequential cooldowns with each standard. The cryogenic measurement network can be summarized with a partial network of error adapters in Figure B1c.

The input paths a_0 and a_1 both have significant attenuation (ϵ_{10} and ϵ_{23}) to prevent room temperature noise from reaching the sample. Because of this, signals directly reflecting off the samples (which are doubly attenuated) are too faint to measure, especially when overlaid on the imperfect return loss on some of the millimeter-wave components in the chain. Instead, we use two separate input paths in order to characterize the response of the sample: when combined, this yields an error adapter network similar to the familiar two-port TRL network [44].

Aside from attenuating terms (ϵ_{10} and ϵ_{23}) and the output amplification (ϵ_{32}) which suffice for a simple correction, we must take into account several non-ideal terms in our error network. As a consequence of highly attenuating inputs is that when normalized, the directivity terms (ϵ_{30} and ϵ_{33}) are significantly more

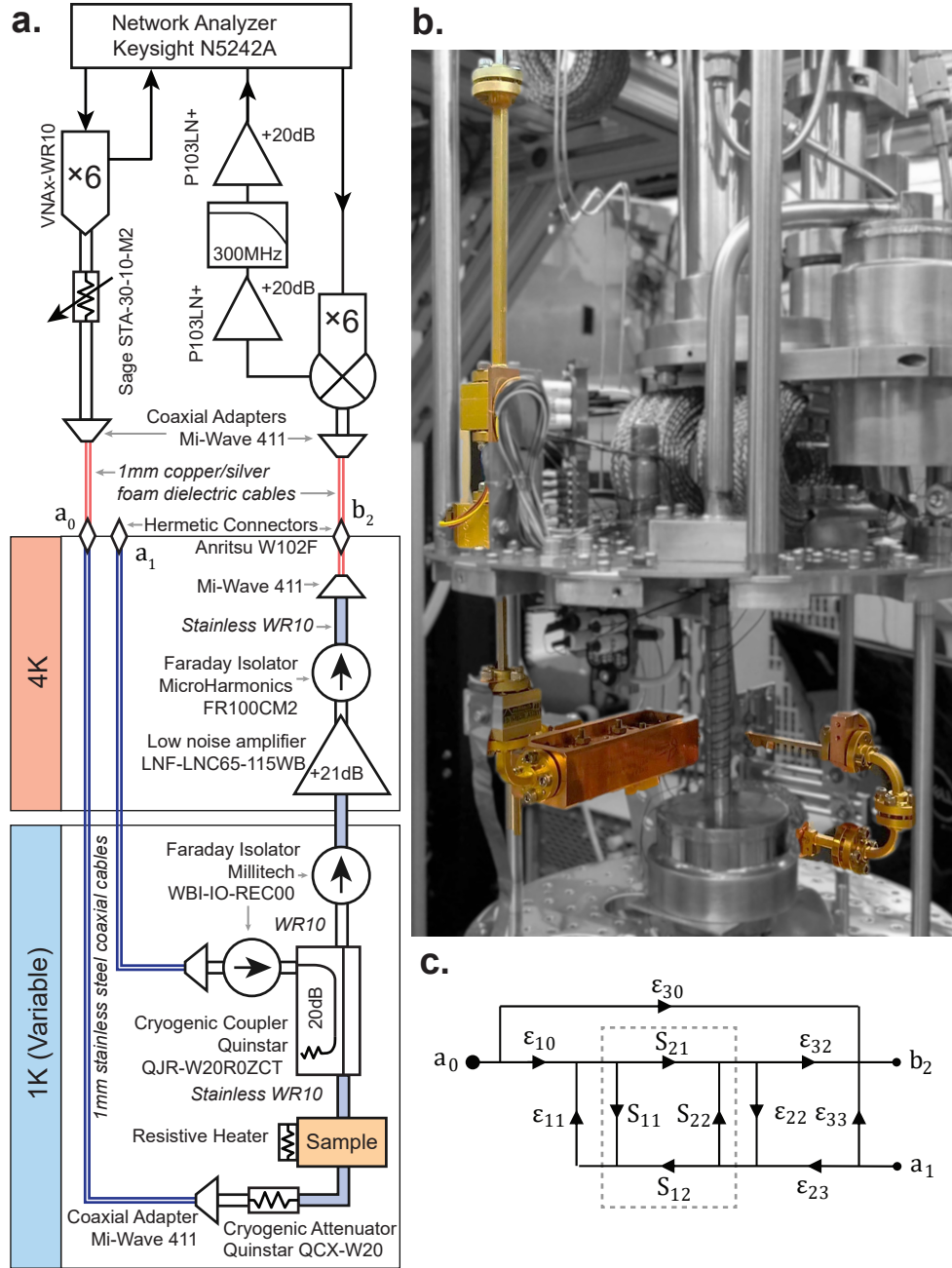


Figure B1. **a)** Schematic of cryogenic millimeter-wave measurement setup. Colored tabs show temperature stages inside the Helium-4 adsorption refrigerator, which reaches a base temperature of 0.86 K. **b)** A photograph highlights relevant hardware inside the fridge. **c)** Adjusted error network used for cryogenic TRL calibrations, where S_x are the respective S-parameters of the sample, and the measurement paths a_0 , a_1 and b_2 are also labelled in the schematic.

pronounced. Additionally, the cryogenic attenuators and absorbers in our system appear have non-ideal return loss characteristics, resulting in non-negligible source match ϵ_{11} and even more pronounced directivity ϵ_{33} . Since we measure good return loss in the cryogenic faraday isolators used on the output line (see Figure B1a), the load match term ϵ_{22} should be significantly less pronounced.

As a result, we can simplify the procedure by

neglecting ϵ_{22} , and make a further assumption that our sample structure is symmetric (in practice this can be checked by reversing the sample direction). These simplifications leave some unresolved frequency ripples on the measured spectrum (visible in Figure 5). The measured transmission and reflection response is now simply:

$$S_{21}^M = \frac{b_2}{a_0} = \epsilon_{30} + \frac{\epsilon_{10}\epsilon_{32}S_{21}}{1 - \epsilon_{11}S_{22}} \quad (\text{B.1})$$

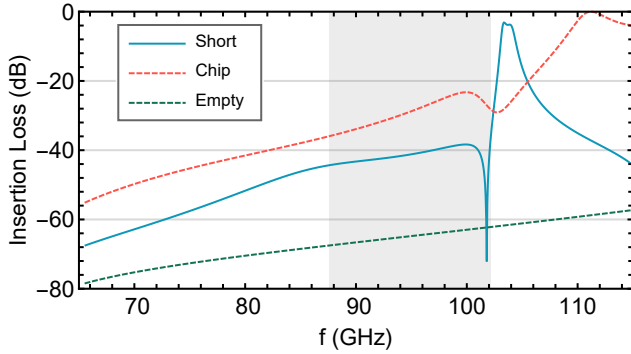


Figure C1. Simulated transmission parameters for: a single transition terminated by an on-chip short, a sapphire chip with no metallization, and the structure with the chip removed. The operating band is highlighted in gray.

$$S_{22}^M = \frac{b_2}{a_1} = \epsilon_{33} + \left(S_{22} + \frac{\epsilon_{11} S_{21}^2}{1 - \epsilon_{11} S_{22}} \right) \epsilon_{23} \epsilon_{32} \quad (\text{B.2})$$

By performing measurements of through, reflect, and line standards which have known S-parameters [44] we can solve this system of equations for relationship the error terms. Combining this with direct measurements of each input line yields true values for each error term. With the system now characterized, we can extract sample S-parameters from the transmission and reflection measurements above, giving a much more accurate picture. Since each measurement now relies on a number of calibration experiments, this imparts a linear error (with typical vector magnitude between 0.03 – 0.09) on the final complex S-parameter. As the amount of measurement uncertainty now depends on the measurements themselves (defined by the relationships in Equation B.1 - B.2), this results in S-parameter uncertainty that increases as the S-parameter decreases, apparent in the significantly higher uncertainty on our reflection measurements.

Appendix C. Leakage Bypassing the Transition

We have thus far treated the system of two back-to-back taper transitions as a single unified network described by a set of S-parameters. However to verify the effectiveness of the transition with even greater precision, the transitions themselves could be de-embedded by defining an error sub-network inside the grey box in Figure B1c. This could help with getting more accurate measurements of more complex on-chip devices, but in particular the isolation term of this sub-network (equivalent to ϵ_{30} in Figure B1c) could shed some light on how much signal passes through the slotline and reaches the resonators as opposed to bypassing the chip entirely. With our measurement precision, the correction method described earlier already gives fairly high uncertainty

without introducing these extra error parameters, so we are unable to directly measure this leakage with good accuracy.

However, we can use simulations (which show fairly good agreement with the measured responses) to estimate the relative magnitude of the leakage. In Figure C1, the solid blue line shows the simulated transmission of a chip with a tapered transition on one side, and entirely covered by uniform ground plane on the other. This measurement corresponds to the *Reflect* standard used in the TRL calibration [44], and directly measures the isolation error term. Thus we find that in the band of interest for our system (highlighted in Figure C1), the simulated leakage is below approximately 38 dB; this value results in a total reduction between 0.05 and 0.1 dB on our measured insertion loss: significantly lower than the uncertainty from calibration discussed in the previous section.

This leakage term is small enough to ignore for resonator measurements, however sheds light on imperfections in this design. To estimate the leakage origin, we also simulate transmission of the geometry with a bare sapphire chip containing no metal, as well as transmission without the chip entirely, shown with dashed lines in Figure C1. From this we conclude that the bare sapphire chip supports modes which help transmit significantly more signal than just the copper enclosure geometry itself. While these spurious modes are suppressed by the surface metal (demonstrated by reduced transmission of the short) a more careful examination could help further improve the transition design.